TUDelft

Delft University of Technology

Ultrafast scanning electron microscopy with sub-micrometer optical pump resolution

Garming, Mathijs W.H.; Weppelman, I. Gerward C.; Lee, Martin; Stavenga, Thijs; Hoogenboom, Jacob P.

Important note
To cite this publication, please use the final published version (if applicable).
Please check the document version above.

ⓘD Mathijs W. H. Garming, I. Gerward C. Weppelman, ⓘD Martin Lee, et al.

COLLECTIONS

Ⓕ   This paper was selected as Featured

View Online   Export Citation   CrossMark

ARTICLES YOU MAY BE INTERESTED IN

Ultrafast scanning electron microscopy with sub-micrometer optical pump resolution Ⓕ

View Online   Export Citation   CrossMark

Mathijs W. H. Garming,[1] ⓘ I. Gerward C. Weppelman,[1] Martin Lee,[2] ⓘ Thijs Stavenga,[1] and Jacob P. Hoogenboom[1,a) ⓘ

AFFILIATIONS

[1]Department of Imaging Physics, Delft University of Technology, Delft, The Netherlands
[2]Department of Quantum Nanoscience, Delft University of Technology, Delft, The Netherlands

[a)]Author to whom correspondence should be addressed: j.p.hoogenboom@tudelft.nl

ABSTRACT

Ultrafast scanning electron microscopy images carrier dynamics and carrier induced surface voltages using a laser pump electron probe scheme, potentially surpassing all-optical techniques in probe resolution and surface sensitivity. Current implementations have left a four order of magnitude gap between optical pump and electron probe resolution, which particularly hampers spatial resolution in the investigation of carrier induced local surface photovoltages. Here, we present a system capable of focusing the laser using an inverted optical microscope built into an ultrafast scanning electron microscopy setup to enable high numerical aperture pulsed optical excitation in conjunction with ultrafast electron beam probing. We demonstrate an order of magnitude improvement in optical pump resolution, bringing this to sub-micrometer length scales. We further show that temporal laser pump resolution can be maintained inside the scanning electron microscope by pre-compensating dispersion induced by the components required to bring the beam into the vacuum chamber and to a tight focus. We illustrate our approach using molybdenum disulfide, a two-dimensional transition metal dichalcogenide, where we measure ultrafast carrier relaxation rates and induced negative surface potentials between different flakes selected with the scanning electron microscope as well as on defined positions within a single flake.

I. INTRODUCTION

Four-dimensional or ultrafast scanning electron microscopy (USEM) has in recent years been pioneered as a promising technique to study temporal dynamics in nanostructured materials with electron beam resolution.[1,2] In USEM, a pulsed laser beam excites (or pumps) the sample while a pulsed electron beam, scanning the sample at a fixed delay with respect to the laser pulse, probes the material response with high resolution.[3,4] The majority of reports to date have targeted the imaging of semiconductor carrier dynamics, creating carriers through fs laser excitation and tracking them with electron probe pulses through a carrier induced change in the secondary electron signal. Materials and specimens whose charge carrier dynamics have been studied with USEM to date include bulk samples of silicon of various doping,[5–7] GaAs,[8] CdSe,[2,9] and alumina.[10] The impressive surface sensitivity of USEM enabled by detection of low-energy secondary electrons also allows for resolving the influence of surface termination on carrier dynamics, as demonstrated on CdTe[11] and GaAs.[12] In addition, the change in the surface potential induced by the presence of photo-excited

free charge carriers can be simultaneously measured with USEM through the local influence of this surface potential on the secondary electron (SE) trajectories and thereby SE collection efficiency.[10,12]

USEM is unique in its combination of direct electron beam microscopy, ultrafast carrier dynamics imaging, surface sensitivity, and surface photovoltage measurement. All-optical transient absorption techniques are traditionally used to measure charge carrier dynamics[13,14] but are limited by light optical diffraction, and the large penetration depth of photons may lead to reduced contrast from thin samples or surface layers. In addition, sensitivity to induced surface photovoltages is lacking. Surface potentials can be measured with Kelvin probe force microscopy,[15] but the scanning probe may be difficult to combine with electron beam imaging of the sample. Time-resolved scanning tunneling microscopy (STM) is another interesting technique capable of surface inspection at high spatial resolution on the ultrafast time scale[16] but also without the electron beam aiding in the selection of measurement areas. Time-resolved photo-emission electron microscopy (TR-PEEM) has a similar contrast mechanism

and, thus, thin-layer sensitivity as USEM,[17,18] but uses high-energy (UV) photons instead of the probing focused electron beam.

In current implementations of USEM, the optical pump resolution is on the order of tens of micrometers, leaving a four order of magnitude gap in resolution compared to the electron pulse beam.[19,20] Most USEM setups are based on a scanning electron microscope (SEM) setup, often a commercial system, that is modified to accommodate fs-laser excitation of the sample and a pulsed electron beam.[2,21,22] Pulsing the electron beam is typically done by applying a scheme, where the electron emitter is photo-excited to generate electron pulses.[23,24] Photo-excitation of the sample is achieved with an optically transparent window in the vacuum chamber with a lens on the air side to focus the laser on the sample from the same side as the incoming electron beam.[19] This enables focusing the laser on samples for pumping, albeit with a large distance between a lens and a sample and, therefore, a very small numerical aperture (NA) that constitutes a limitation for achievable optical resolution.

Better focusing of the laser has the potential of greatly improving measurement resolution. As the spatial resolution for USEM measurements probing a semiconductor surface photovoltage (SPV) is limited by the size of the laser beam focus, and not the electron beam probe, it is useful to decrease the size of the laser spot in order to probe surface potentials over smaller areas. This would enable measuring on specific sections of samples and devices, rather than bulk wafers, and be particularly useful for measurement of 2D materials. In addition, for very small regions of interest, such as nanoparticles, reduction in the laser spot size would have the added benefit of only exciting the measurement area without the risk of exposing and possibly modifying the surrounding area. In contrast, current implementations have targeted ensembles of nanoparticles all pumped at the same time.[25–28] Furthermore, a more tightly focused laser spot results in a higher power density; an improvement from a 30 μm spot to a diffraction limited sub-micrometer excitation area would entail roughly a thousand times higher laser fluence on the sample. An improvement in this magnitude would require the addition of (high-NA) optics in the SEM vacuum chamber, which may interfere with an electron beam and signal trajectories and add considerable dispersion to the laser pump pulse potentially compromising temporal resolution.

Here, we present a USEM setup with an integrated inverted optical microscope, utilizing high-NA microscope objective lenses akin to those used in conventional optical microscopes. By bringing all the optics inside the vacuum, the optical working distance is much lower than in the conventional case, and this enables sub-micrometer optical excitation and imaging of the sample, constituting a major step forward in resolution. The light optical objective lens is located below the sample,[29,30] such that it does not interfere with electron microscopy and allows investigation of nanoscale materials on transparent substrates. We show that spatial and temporal resolution can be maintained in the vacuum chamber by pre-compensating dispersion of a vacuum window (VW) and an objective lens and demonstrate our high-NA USEM setup with ultrafast movies of carrier dynamics on thin molybdenum disulfide (MoS$_2$) flakes probing both selected individual flakes as well as specific locations within a single micrometer-scaled MoS$_2$ flake.

II. EXPERIMENTAL SECTION

High-NA excitation is implemented in our SEM-based setup, as shown in Fig. 1, which also displays a typical state of the art USEM setup for comparison. The vacuum door and sample stage in a FEI Quanta 200 FEG microscope have been replaced with a custom built inverted optical microscope that accommodates conventional optical objectives. The sample holder, mounted on a piezostage, has an opening over which samples are mounted to ensure optical access. We previously used the integrated high-NA objective lenses for detection of e-beam induced cathodoluminescence.[30–33] Here, we add an optical excitation path to pump the sample with all components except for a mirror and the objective lens outside the vacuum chamber. The vacuum window facilitating this is a 10-mm-thick optical flat (CVI Melles Griot). Secondary electrons (SEs), forming the probe signal, are detected with an Everhart–Thornley detector (ETD) positioned in its standard configuration in the sample chamber.

The optical excitation path from the laser to the sample is shown in Fig. 2. The laser is a Coherent Vitara-T with 800 nm center wavelength and 95 MHz pulse repetition frequency. Sub-20 fs pulse duration is possible with the bandwidth at the widest setting of 125 nm. All optical components, particularly the vacuum window and the objective, introduce frequency dispersion to our broadband optical pulses, causing temporal broadening. We compensate for this with a set of dispersion compensation mirrors, which allow us to add negative dispersion and retain an ultrashort pulse at the sample. Optical power is regulated with a neutral density filter and a combination of a rotatable half lambda plate and a Brewster wedge based polarization filter. A beam expander with 3.75:1 ratio broadens the beam to fill more of the back aperture of objectives and make better use of their high NA; for these experiments, we use a Nikon 40× objective with 0.95 NA or a 40 × 1.25 NA water immersion objective in combination with vacuum compatible immersion fluid. The path also contains a beam chopper for lock-in detection.

The laser-induced SE signal is modulated by the beam chopper periodically blocking the laser at a 940 Hz chopping frequency, which allows us to extract it from the total SE emission signal with a lock-in amplifier (Fig. 2). Thus, we do not need to use reference image subtraction[7,34,35] with the additional advantage of simultaneously visualizing processes slower than the pump–probe repetition time such as trapping of carriers.[12] Furthermore, in this way, we mitigate drift in the alignment or sample position between the recordings of reference and other images.

Electron beam blanking is used to pulse our electron beam, as detailed in Ref. 31. Briefly, the continuous electron beam from a standard source is chopped by the beam blanker rapidly deflecting it over a blanking aperture. This solution of pulsing an electron beam predates the laser triggered source but has recently found more use in various forms.[24,36–38] While some blanker designs have longer pulse durations than phototriggered sources,[37] advantages include less invasive implementation in the microscope and improved stability during use as we are not sensitive to drift of the source vs the laser illumination. Furthermore, the laser power does not have to be divided between the electron source and sample. A pulse duration below 100 ps can be achieved at 4 kV acceleration voltage in our setup[31] with a linear relation between the pulse width and acceleration voltage. The use of a conjugate blanking scheme where the beam is focused between the blanker plates ensures that spatial resolution of the electron beam is preserved,[31] and blanker induced spot displacement and blur is negligible.[39] We use a standard 5 Vpp square wave function generator to drive the beam blanker, resulting in an electron pulse for the rising and for the falling edge of the signal.
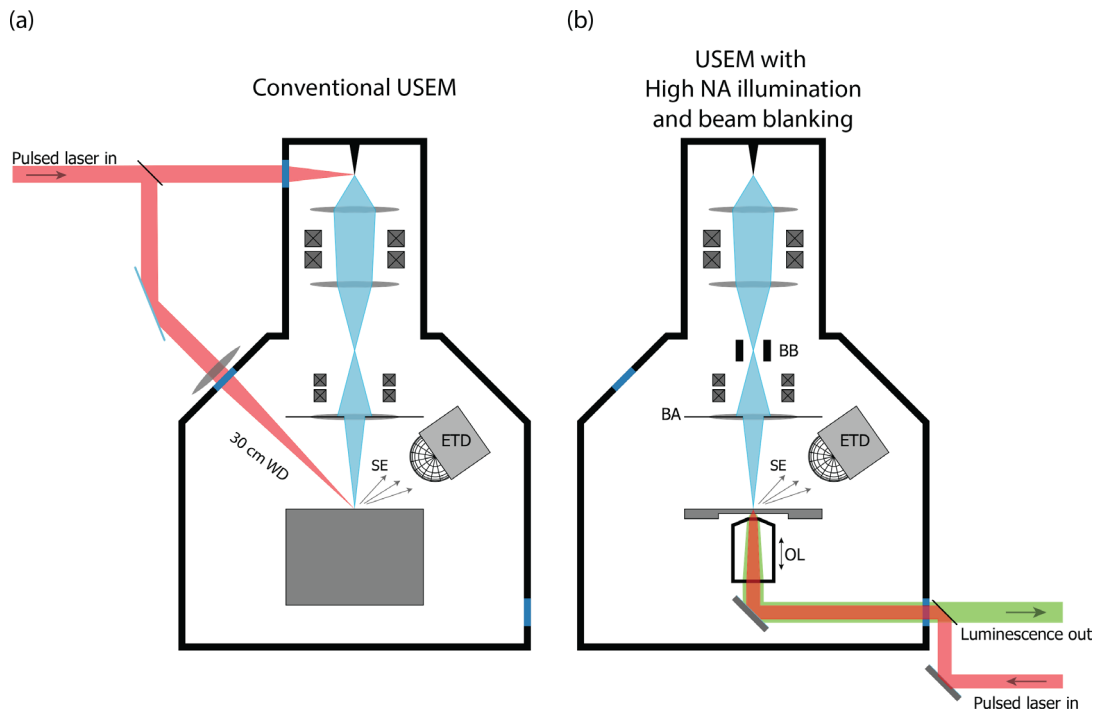
FIG. 1. Integrated inverted optical objective allows for high-NA pulsed laser excitation. (a) Typical state of the art USEM setup with a laser triggered electron source. (b) High-NA USEM setup with a custom built inverted optical microscope for photoexcitation of the sample with high-NA objective lens (OL) at diffraction limited resolution. A beam blanker (BB) with blanking aperture (BA) is used, negating the need to (partially) direct the laser to the electron source for pulsing the electron beam. Secondary electrons are detected as the probe signal with an Everhart–Thornley detector (ETD).
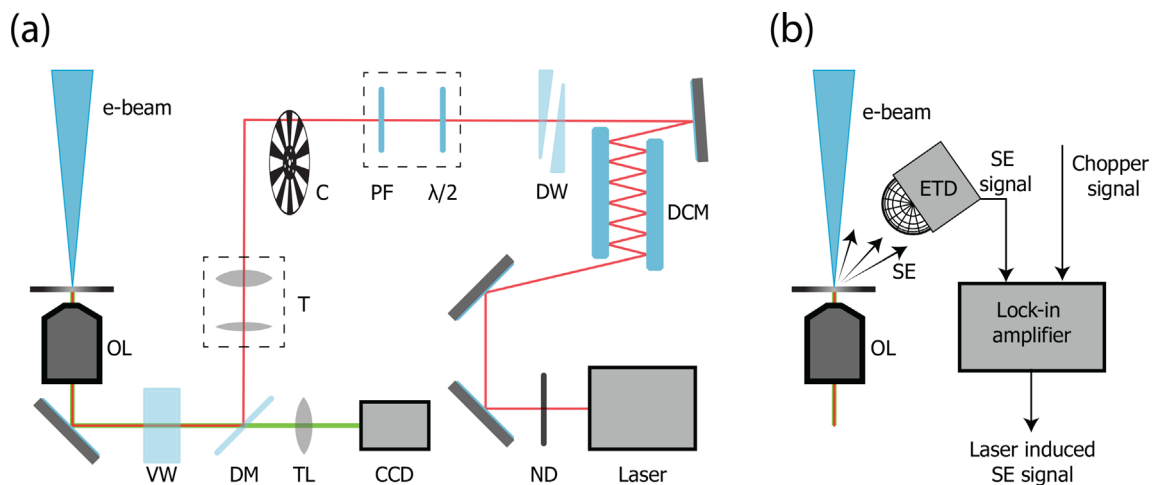
FIG. 2. Dispersion compensation optics are used in the excitation path and lock-in detection in the detection path. (a) The pulsed laser beam (95 MHz, 800 nm) first goes through a neutral density filter (ND) to regulate power before entering dispersion compensation mirrors (DCMs) and dispersion wedges (DWs). Next are a half lambda plate (λ/2) and a polarization filter (PF) controlling power and polarization, beam chopper (C) for lock-in detection, 3.75:1 beam broadening telescope (T), dichroic mirror (DM), vacuum window (VW), and objective lens (OL). A tube lens (TL) and a CCD camera are used for imaging of the sample. (b) Lock-in detection is implemented by feeding the ETD signal to a lock-in detector to extract the laser induced SE signal from the total SE signal.

(a)

(b)
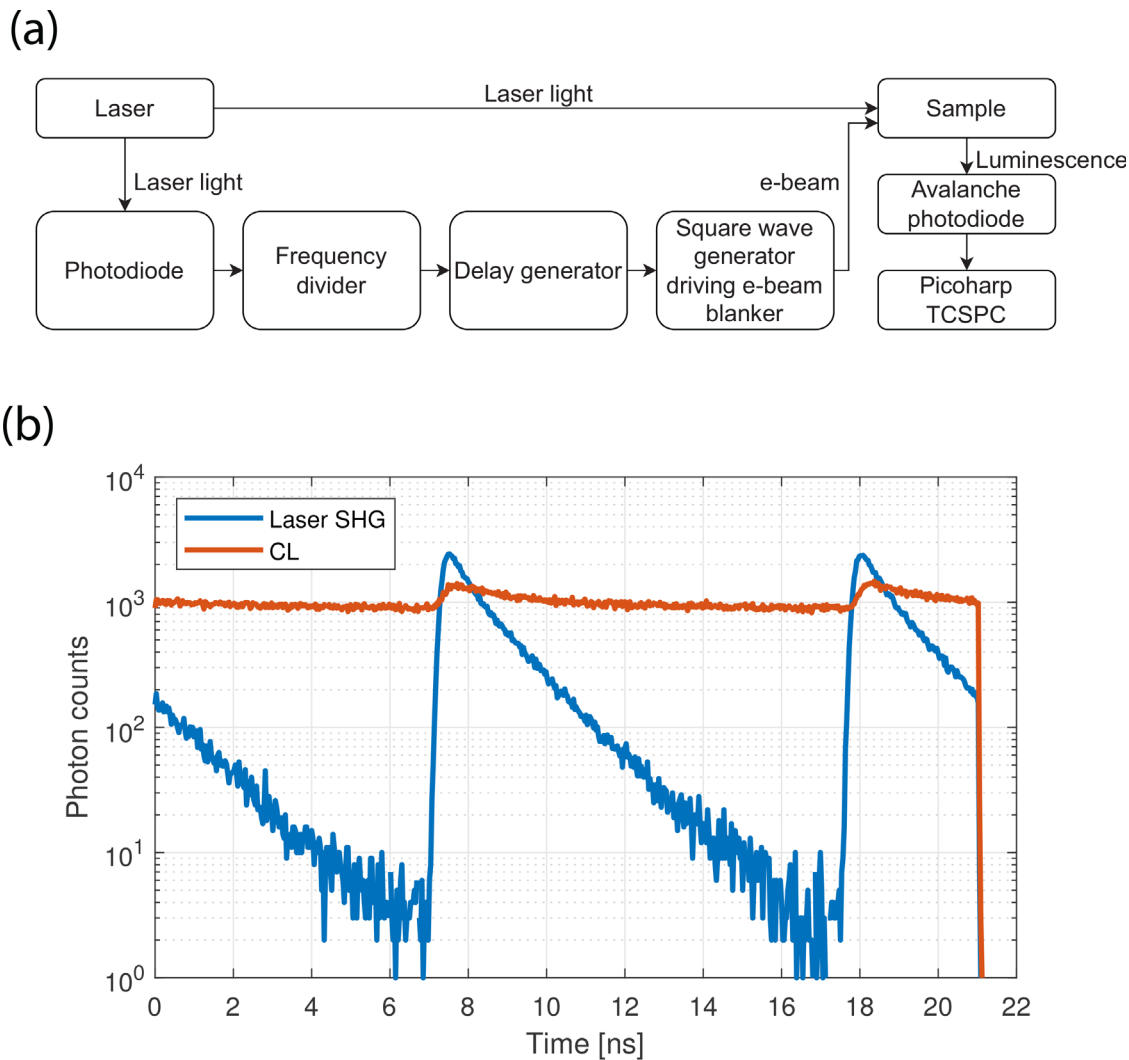
FIG. 3. Timing of the laser and electron pulses can be monitored with time correlated single photon counting (TCSPC), enabling sub-ns temporal alignment. (a) Electron pulse generation is synchronized to the laser pulses by using a laser generated triggering signal on the square wave generator driving the blanker. The laser illuminates a photodiode, whose output signal is sent through a frequency divider and a delay generator before triggering the blanker signal generator. Pulse arrival times are monitored by measuring luminescence from the sample with an avalanche photodiode (APD) and a time correlated single photon counting unit. (b) Logarithmic arrival time histogram of electron beam generated cathodoluminescence and laser reflections measured with time correlated single photon counting. Pulse shapes are the result of a convolution between intrinsic pulse shape and the instrument response primarily determined by the APD and measurement circuit. The timing of the electron pulse generation is adjusted such that the electron beam and laser signals have the same arrival time.

Accurate synchronization of the laser and electron pulses in time is crucial in achieving temporal resolution. As a beam blanking solution does not yield the same natural synchronization of the pulse repetition frequency as laser triggered sources do, we implemented an alternative procedure. As schematically represented in the block diagram in Fig. 3, electron pulses are locked to the laser pulse train by triggering the square wave generator driving the blanker plates with the signal of a photodiode exposed to the laser. A frequency divider halves the frequency of the triggering signal to account for the rising and falling edge of the square wave, ensuring the repetition frequencies of the laser and electron pulses are identical. Delays can be introduced to the triggering signal with a SRS DB64 coax delay box, and fine

adjustments in delay and duty cycle can be made on the square wave generator itself.

Calibration of the pump–probe delay is based on a time correlated single photon counting (TCSPC) scheme. We use an avalanche photodiode (APD) to detect light emitted from the sample, and a PicoHarp 300 TCSPC timing unit to register the arrival time of photons relative to the photodiode signal. For this, we measure the electron-beam induced cathodoluminescence via the objective used for illumination and compare this signal to the arrival time of laser pulse reflections or second harmonic generation (Fig. 3). Zero time delay is found by adjusting the delay in the trigger signal for electron pulse generation such that the arrival time of the laser and CL light coincide.

Some timing jitter is present in this scheme, for example, from the triggering of the pulse generators. However, pulse durations of 90 ps have been measured on this setup,[31] forming an upper limit to the jitter that is much smaller than the timescale of dynamics reported here.

An ultrafast movie is recorded by focusing the laser on the sample (fluence ∼2 mJ/cm^2) and scanning the photo-excited area with a 10 kV acceleration voltage pulsed electron beam. Typical pixel dwell times are on the order of 1 s, comprising many pump–probe cycles. We record the direct SE detector signal as well as the lock-in signal to reconstruct both the total SE signal and the laser induced component of it. The area is scanned multiple times with different pump–probe delays in random order to prevent misinterpretation of sample degradation as ultrafast dynamics. For more information on sample degradation resulting from prolonged exposure, we refer to the supplementary material.

The MoS$_2$ samples are prepared using mechanical exfoliation of naturally occurring bulk crystal (SPI) with tape followed by polydimethylsiloxane (PDMS) (Sylgard 184) stamping[40] on a substrate of ITO covered glass (Optics Balzers). We use two different samples, after stamping sample 1 goes through a cleaning procedure consisting of 1 h in anisole, 1 min in isopropylalcohol (IPA), drying with a blast of nitrogen, 2 h in vacuum oven at 200°, and 4 min of oxygen plasma cleaning at 300 W with faraday cage. Sample 2 was prepared with the same stamping process, but the cleaning steps were omitted. Based on

optical inspection, measured flakes are all many layers (tens of nm) thick, and therefore, their properties will resemble those of bulk MoS$_2$.[41] In addition, we note that the thickness of the sample is much thinner than the optical penetration depth of MoS$_2$ at our 800 nm laser wavelength; the optical absorption is, therefore, in good approximation, constant over the sample thickness.

Spatial resolution of the pump laser is characterized using two-photon luminescence from an InP nanowire. The nanowire sample was prepared by transferring the wires (Bakkers lab, TU/e) from the growth substrate to an ITO slide with lint free tissue. The laser is focused on the sample, which is scanned through the laser spot on a piezostage while the second harmonic signal is recorded on an avalanche photodiode with a 400/40 bandpass filter. The laser spot size is determined from the resolution of the resulting second harmonic image.

Assessment of the temporal resolution of the pump laser is done by means of second order autocorrelation traces, from which the laser pulse duration can be determined.[42,43] The autocorrelation traces are measured using a Michelson interferometer with a 100 μm thick Beta Barium Borate (BBO) crystal (Eksma optics) in the focus of the objective as a second harmonic generator. In the interferometer, the laser beam goes through a beam splitter and one pulse picks up a variable delay in an optical delay line. Both beams are subsequently recombined and focused on the BBO sample, whose second harmonic signal is measured using a photomultiplier tube. With the second harmonic signal intensity
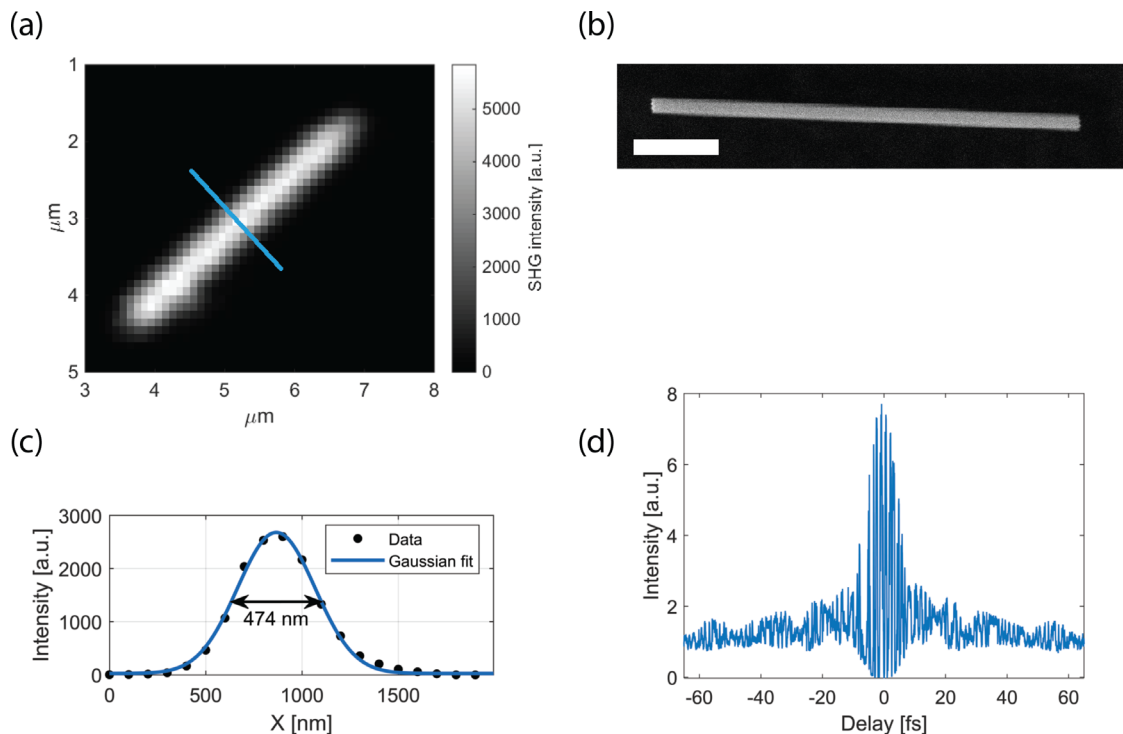
FIG. 4. 620 nm spatial and 15 fs temporal optical pump resolution inside the ultrafast SEM. (a) Two-photon excitation image of a 175 nm diameter InP nanowire acquired by scanning the nanowire through the laser spot. (b) SEM image of an InP wire. (c) Cross section over the line in image (a) with Gaussian fit. The FWHM of the fit is equal to 474 nm, corresponding to a laser spot size of 620 nm in the focal plane. (d) Second order autocorrelation measured with a BBO crystal in the focal plane of the objective lens and with a laser bandwidth of 125 nm. Some higher order dispersion is visible in the trace with this high bandwidth, but the ratio of the peak to background is approximately 1:8 as expected, and we measure a 15 fs pulse duration after dispersion compensation. Scale bar is 1 μm.

proportional to the square of the laser intensity (fourth power of an electric field), the second harmonic signal is up to eight times higher when the pulses overlap in time compared to when they arrive separately.

III. RESULTS

A. Spatial and temporal optical probe size

The spatial extent of the laser pump profile is measured using the two-photon excited signal from an InP nanowire, see Figs. 4(a)–4(c). We fit a Gaussian profile [Fig. 4(c)] to a cross section of the second harmonic image [Fig. 4(a)] and extract 474 nm full width at half maximum (FWHM). We deconvolve this with the wire width [175 nm, Fig. 4(b)] and multiply by $\sqrt{2}$ to arrive at a laser spot size of about 620 nm FWHM with the 1.25 NA 40 × water immersion objective. Thus, we conclude that we have reached sub-micrometer optical pump resolution.

The second order autocorrelation trace, measured to assess the laser pulse duration, was acquired with 125 nm laser bandwidth. Figure 4(d) shows the measured correlation function after 32 bounces of the incoming laser beam through the dispersion compensation mirrors. We retrieve a pulse duration of 15 fs on the sample. Thus, the ultrashort pulse duration can be retained despite the dispersion introduced by the objective lens and vacuum window. Consequently, the laser pulse duration will not limit the temporal resolution of the pump–probe scheme, and the efficiency of multi-photon processes,

such as the generation of second harmonics used for the laser spot size characterization, is maximized. Furthermore, the full toolbox of optical pulse shaping techniques and pulse train formation is available in the SEM vacuum.

B. Ultrafast dynamics

An ultrafast movie of the laser induced SE signal acquired with USEM on a single MoS$_2$ flake is shown in Fig. 5(a). At 0 ns pump–probe delay, a dark spot and an adjacent bright spot are observed; a cross section of this dipolar profile is shown in Fig. 5(b). A double Gaussian fit indicated as a guide to the eye is found to reproduce the data well. The transition between the minimum and maximum intensity of the fitted curve exhibits a 25–75 edge width of 750 nm, close to the above established resolution limit of our high-NA optical pump scheme.

For increasing pump–probe delay, the contrast gradually recedes until it has almost disappeared at −1 ns (equivalent to +9.5 ns at 95 MHz). The dark contrast is more intense compared to the brighter area. In Fig. 5(c), contrast is plotted as a function of the pump–probe delay, where data points show the mean of the five darkest pixels in the ultrafast movie frames after applying a $\sigma = 2$ px Gaussian filter to the raw data and normalizing between −1 and 0. Fitting to an exponential decay $y = -\exp(-x/a)$ results in a 3.2 ns relaxation time

(a)

(b)   (c)
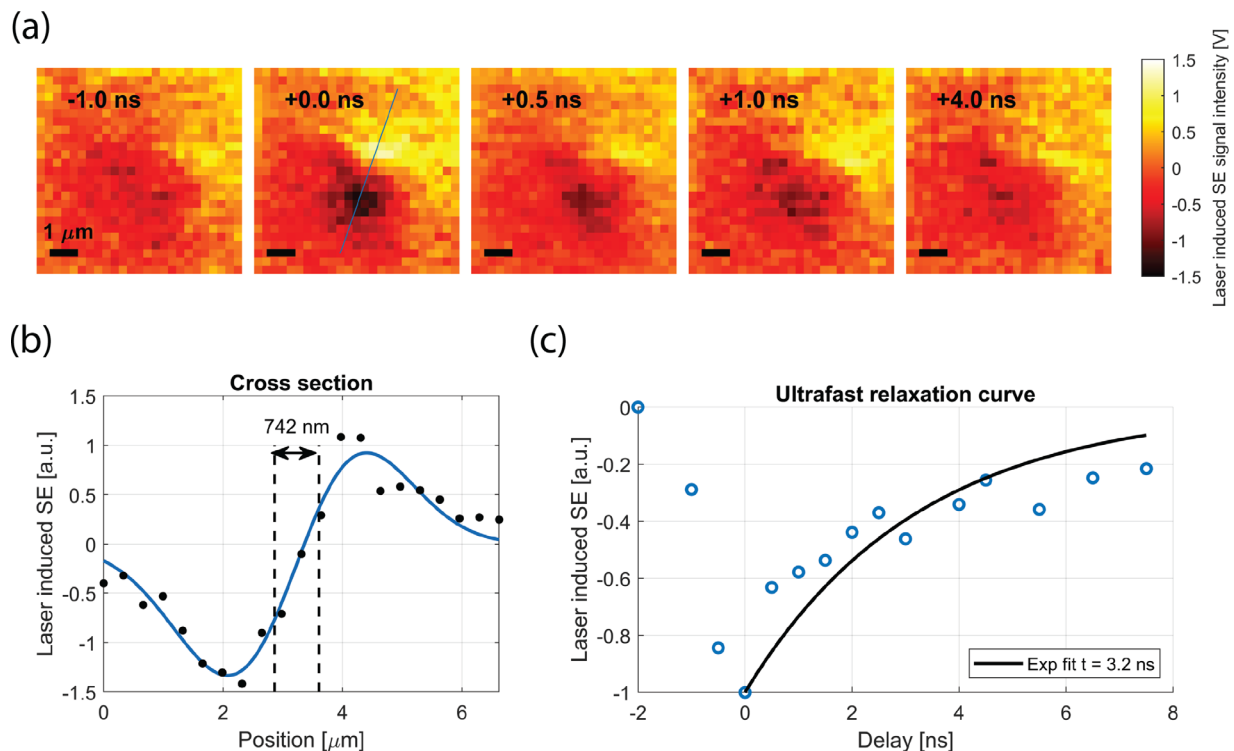
FIG. 5. Ultrafast scanning electron microscopy with sub-micrometer optical pump resolution. (a) Ultrafast movie from an MoS$_2$ flake, showing SE contrast from the laser irradiated area as a function of laser pump-electron probe delay. A dark and bright spot reminiscent of a carrier-induced surface voltage is observed upon laser irradiation, which decays on a few ns time scale. (b) Intensity profile for the laser-induced SE signal at 0 ns delay over the line indicated in the corresponding panel in (a). The solid line shows a double Gaussian fit to the data revealing a 25–75 resolution of 750 nm. (c) Lock-in signal, i.e., laser induced SE signal as a function of the pump–probe delay. The single-exponential fit to the rising part of the curve yields a recovery time of 3.2 ns.
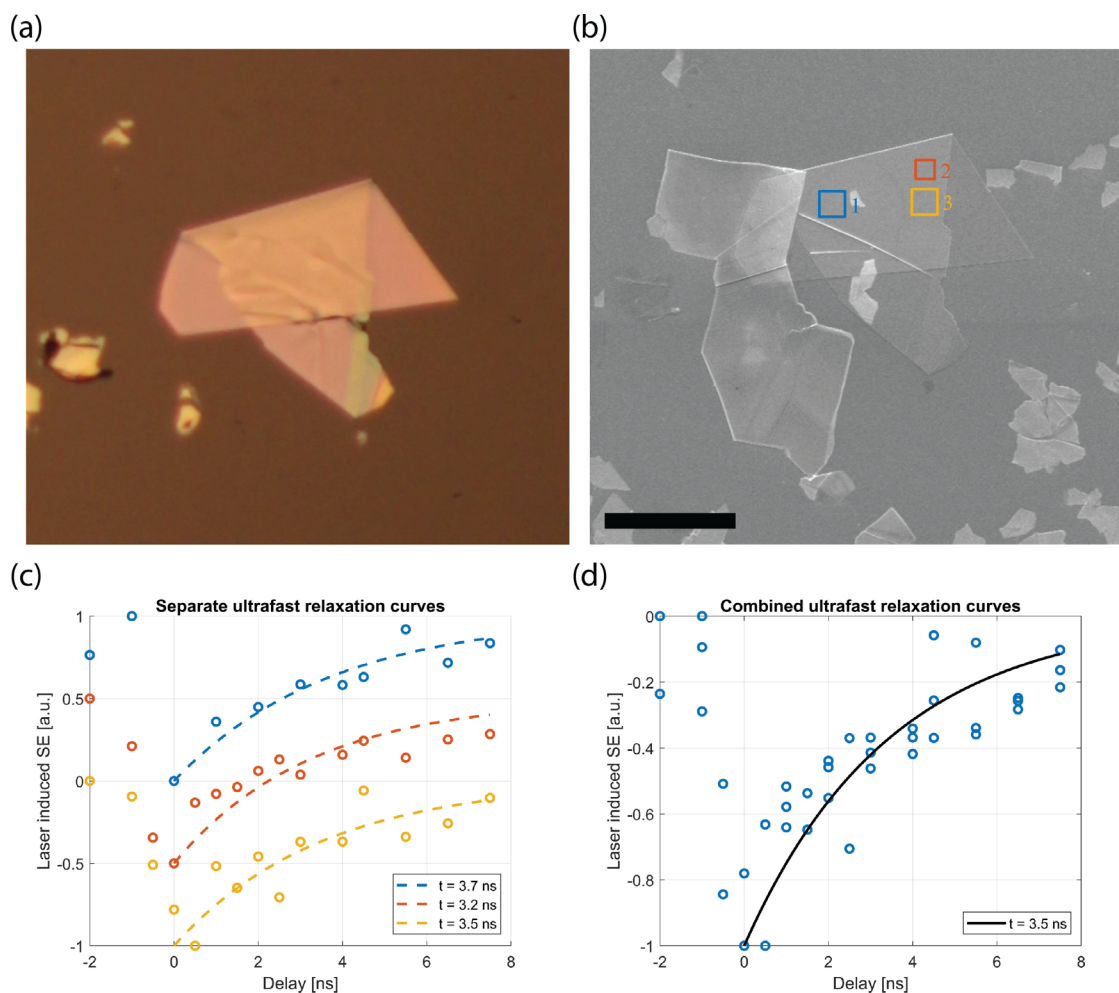
FIG. 6. Localized sub-micrometer optical pump excitation on pre-selected areas within a single MoS$_2$ flake. (a) Optical image of an MoS$_2$ flake on PDMS stamp recorded during sample preparation and (b) an SEM image of the same flake after stamping on ITO coated glass. Marked regions have been selected for recording ultrafast movies. (c) Laser-induced SE signal from the areas marked in (b) as a function of the delay time. Curves have been normalized and offset for clarity. Dashed lines indicate exponential fits with lifetimes indicated (blue for region 1, red 2, yellow 3). (d) All data points combined into a single fit, showing 3.5 ns lifetime. Despite some variation in the individual curves, they collectively yield a lifetime value very close to the photoluminescence lifetime of bulk MoS$_2$. Scale bar in (b) indicates 50 μm.

constant. We note, however, that we observe rather large 95% uncertainty bounds for this fit of (2.4, 4.1) ns.

The above-mentioned result was obtained by pumping a sub-micrometer area on a MoS$_2$ flake tens of micrometers in size. We repeated this measurement on different areas of the same flake, thus showing how our high-NA USEM setup allows micrometer-scale site-selective excitation. Figure 6(a) shows an optical image of the examined flake while on the PDMS stamp, while Fig. 6(b) shows a SEM image of the same flake after deposition on the ITO-sample. The SEM image shows more flakes as the sample was stamped multiple times to deposit additional flakes. Region 2 indicates the area selected for recording the dynamics in Fig. 5. The additional areas are labeled as 1 and 3. These yield similar ultrafast movies with ns-scale dynamics with decay constants of 3.7 (2.9, 4.6) and 3.5 ns (2.3, 4.7) [Fig. 6(c)]. When the data points are normalized and fitted together as shown in Fig. 6(d), a time constant of 3.5 (2.9, 4.0) ns is found. This is in

agreement with the few ns lifetime reported in the literature for bulk MoS$_2$ based on transient absorption measurements, optical-pump THz-probe measurements, and first principles calculations of exciton lifetimes,[44–46] and we, therefore, associate this decay with carrier recombination.

We next conducted additional measurements on different MoS$_2$ flakes on another sample in the experimental section referred to as sample 2. In order to expedite the measurements and focusing on the temporal information, we implemented a faster acquisition scheme for recovering the ultrafast dynamics. Instead of recording full scan images like in Fig. 5, the electron beam is rapidly scanned over a 1 square micrometer area of the laser spot, and we record the 5 s average laser induced SE signal from the lock-in detector at every delay. We cycle through the delay settings four times and take the mean for each pump–probe delay to get a decay curve. This is done on four regions of interest on three different flakes. We find lifetimes of 2.2 (1.6, 2.7),
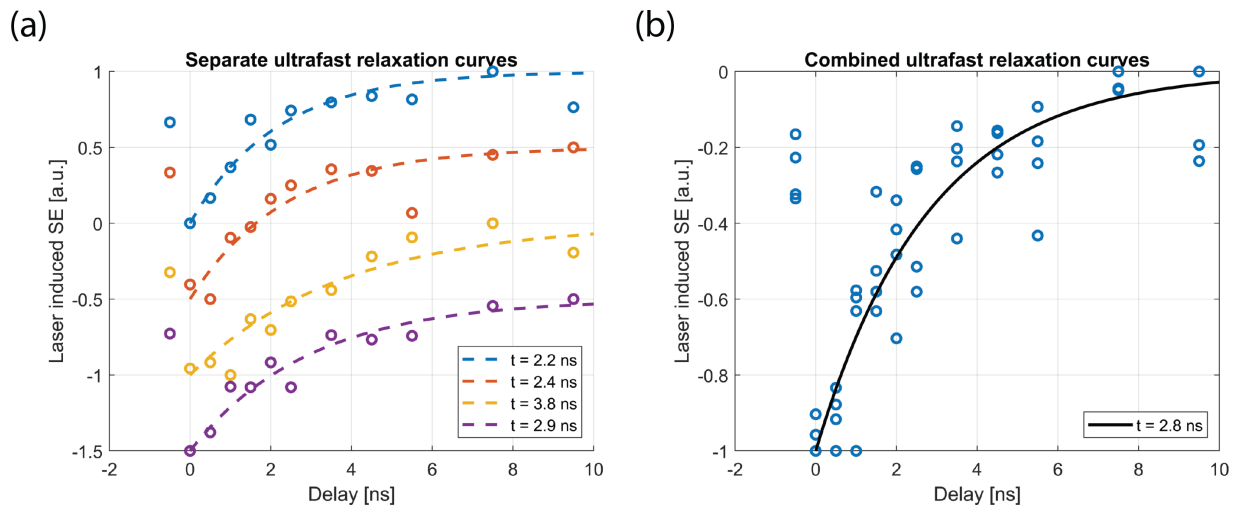
FIG. 7. Decay curves measured on multiple flakes consistently show ns-scale recovery. (a) The decay curves of four separate regions on three different MoS$_2$ flakes of sample 2 all show ns scale recovery. The variation in fitted decay times spreads from 2.2 to 3.8 ns with mostly overlapping confidence bounds (see the text). (b) When combining the curves into a single fit, a lifetime close to the literature value emerges again.

2.4 (1.5, 3.2), 3.8 (2.7, 4.8), and 2.9 (2.3, 3.5) ns [Fig. 7(a)]. These values are in correspondence with the range of values observed for the previous sample. Combining the data points into a single fit [Fig. 7(b)] results in a 2.8 (2.4, 3.2) ns time constant. We conclude that we observe a spread in charge carrier lifetimes measured with USEM of about 2.2 to 3.8 ns both for measurements between different flakes as well as within single flakes, and most of the uncertainty bounds are overlapping. As non-homogeneities can affect dynamics, we note that the measurement areas we selected on the flakes always appeared homogeneous in SEM and did not visibly overlap with edges or step variations in height, and contained no visible markings, scratches, or defects [see also Fig. 6(b)]. Possibly, sample variations not visible in SEM imaging have still affected the measured lifetimes.
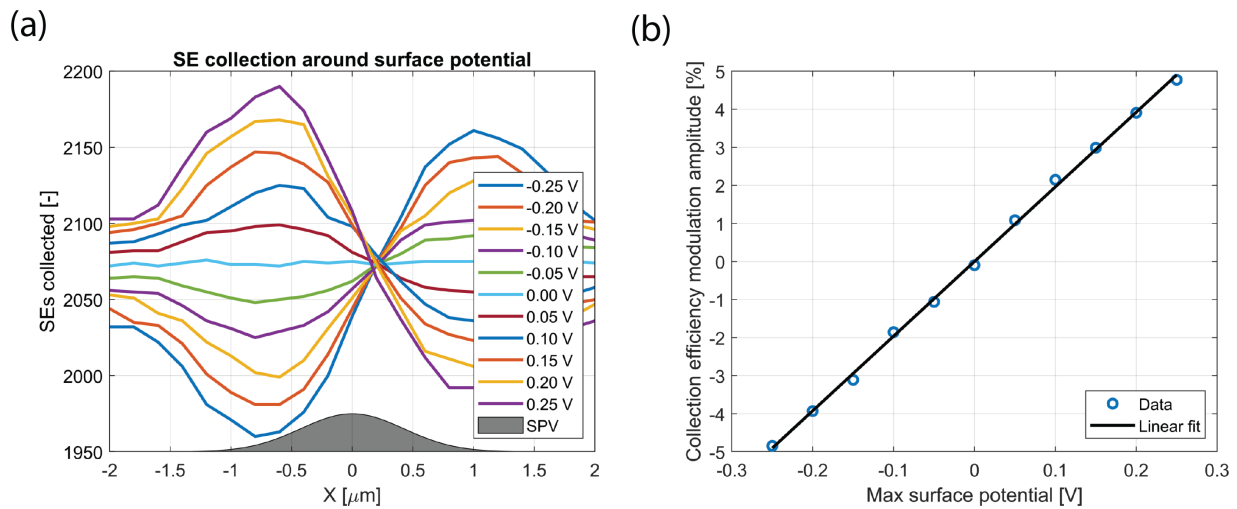
C. Dipolar USEM contrast pattern

We next turn our attention to the dipolar dark and bright contrast observed in the USEM image sequence on MoS$_2$ (Fig. 5). We have previously shown on GaAs that carrier induced surface photovoltages (SPVs) can result in such a dipolar contrast extending over a tens of micrometers laser pump size.[12] The process of forming this surface potential through band bending and its effect on SE yield of the sample is discussed in detail by Li *et al.*[47] In addition to a yield change, a local surface potential influences SE trajectories, creating the dipolar patterns through the interplay between the SPV and asymmetry in the detector positioning.[10,12] Both the surface potential and the voltage on the grid of the ETD (positioned north relative to the scanning direction in our setup and the image orientation in Fig. 5) affect the trajectory of low energy SEs; the surface potential can either collaborate with the ETD grid to guide SEs in the direction of the detector leading to a brighter than background contrast, or the surface potential negatively influences the local detection efficiency. This contrast then depends on the release position of the SEs relative to the SPV.[10,12]

We first confirm that the above interpretation of the dipolar contrast pattern also holds for sub-micrometer scale SPV areas. To this

end, we conducted simulations in COMSOL using the electrostatics and particle tracing interfaces to fly particles through a 2D geometry representing the vacuum chamber. Particles are released 10 nm above the surface at various release positions around the surface potential with an energy distribution representing the SE spectrum of silicon and directions drawn from a 2D Lambert cosine distribution. We record the number of electrons reaching the detector. The SE collection efficiency as a function of the release position and SPV value is given in Fig. 8(a). For all voltages, we see a dipolar pattern appearing that is similar in shape to what was found experimentally (Fig. 5), and in Fig. 8(b), it is seen that the intensity of the dipolar profile scales linearly with the surface potential. Based on these results, we conclude that the measured dipolar pattern originates from a negative surface potential. We note that the appearance of a negative surface potential after MoS$_2$ carrier excitation is probably due to a thin carbon contamination layer formed on top of the MoS$_2$ after electron beam exposure (see also the supplementary material).

Based on the simulation results in Fig. 8, an estimate of the magnitude of the surface potential could be made, but we note that this would only constitute a coarse approximation for three reasons. First, we have assumed the intensity profile of the surface potential to follow that of the laser, i.e., Gaussian, but diffusion of carriers and saturation effects could lead to a more complicated spatial profile. Second, the simulation only takes into account the secondary electrons released at the primary beam position, the so-called SE1 electrons. In reality, backscatter electrons induce SE emission from other parts of the sample as well as other surfaces such as the pole piece and the vacuum chamber walls. These SE2 and SE3 contributions to the total SE signal do not have the same dependence on surface potential and, therefore, reduce the relative change in the total SE signal compared to the simulated SE1 signal by up to as much as a factor 3.[48] Third, the modeled SE energy spectrum, SE release direction, and geometry of the vacuum chamber are approximations. Therefore, to quantitatively measure the magnitude of the surface potential with USEM, calibration would be

FIG. 8. Simulations show a micrometer-scale local surface potential can create dipolar USEM contrast pattens with intensity scaling linearly with voltage. (a) Simulated number of electrons collected by the detector as a function of the release position relative to the center of the surface potential, for varying surface potential voltages. Spatial extent of surface photovoltage shown in gray. The detector is positioned in the positive x direction. (b) Modulation amplitude in percent as a function of the surface potential with linear fit.

required. Without independent calibration, temporal variations in induced surface potential can be monitored thanks to the linear relation between the surface potential and SE signal modulation.

IV. CONCLUSION

We have built and demonstrated a new implementation for USEM in which the sample is laser illuminated from below allowing for improved spatial pump resolution compared to existing implementations. We use dispersion compensation to retain ultrashort, tens of fs, laser pulses in the sub-micrometer focus of a high-NA optical objective. This narrows the gap between the laser optical and electron optical resolution in USEM, allowing us to probe fs-laser excitation induced surface photovoltages over areas as small as a few hundreds of nm in wide. Our laser illumination scheme is particularly suitable for thin or transparent samples, including nanoparticles that can be deposited on transparent substrates and 2D materials such as MoS_2, which we have used to demonstrate the capability of measuring high resolution ultrafast movies of carrier relaxation and carrier induced surface potential dynamics. The addition of an optical parametric oscillator (OPO) and pulse picker to the laser setup has the potential to further generalize the method to be applicable to high bandgap materials and long recombination time semiconductors.

High-NA USEM enables single and sub-micrometer light optical pump scales, enhancing the possibilities for measuring carrier dynamics in nanostructured devices and materials. Further studies could, for instance, target sections of 2D materials with specific thickness, or measure across steps, defects, and junctions. The applicability to transition metal dichalcogenide materials also provides the interesting prospect of evaluating (hetero)layered semiconductor devices. In addition, the use of conventional microscope objectives for excitation also makes it possible to combine USEM with optical imaging of the sample. Region of interest selection based on optical signals would be another possibility, as is further manipulation of the optical

stimulation, e.g., with polarization control, super-resolution, and pulse shaping. This will further increase our possibilities for assessing photo-excited carrier dynamics in and around semiconductor nanodevices, ultimately aiding the optimization and development of novel tools, for example, for photodetection and photovoltaics.

SUPPLEMENTARY MATERIAL

See the supplementary material for the USEM measurements with different electron beam current and dose investigating the effect of sample degradation after prolonged exposure.

AUTHOR DECLARATIONS
Conflict of Interest

The integrated light microscope served as a prototype for a product of Delmic BV in which J.P.H. has a financial interest. The authors have no conflicts to disclose.

Author Contributions

Mathijs W. H. Garming: Conceptualization (equal); Data curation (lead); Formal analysis (lead); Investigation (lead); Methodology (lead); Software (equal); Writing – original draft (lead); Writing – review and editing (equal). **I. Gerward C. Weppelman:** Conceptualization (equal); Investigation (supporting); Methodology (equal); Writing – review and editing (supporting). **Martin Lee:** Formal analysis (supporting); Resources (equal); Writing – review and editing (supporting). **Thijs Stavenga:** Data curation (supporting); Methodology (supporting); Writing – review and

editing (supporting). **Jacob P. Hoogenboom:** Conceptualization (lead); Funding acquisition (lead); Methodology (supporting); Project administration (lead); Supervision (lead); Writing – original draft (supporting); Writing – review and editing (lead).

REFERENCES

[1]A. H. Zewail, "Four-dimensional electron microscopy," Science **328**(5975), 187–193 (2010).

[2]O. F. Mohammed, D. S. Yang, S. K. Pal, and A. H. Zewail, "4D scanning ultrafast electron microscopy: Visualization of materials surface dynamics," J. Am. Chem. Soc. **133**(20), 7708–7711 (2011).

[3]J. Sun, A. Adhikari, B. S. Shaheen, H. Yang, and O. F. Mohammed, "Mapping carrier dynamics on material surfaces in space and time using scanning ultrafast electron microscopy," J. Phys. Chem. Lett. **7**(6), 985–994 (2016).

[4]G. M. Vanacore, A. W. P. Fitzpatrick, and A. H. Zewail, "Four-dimensional electron microscopy: Ultrafast imaging, diffraction and spectroscopy in materials science and biology," Nano Today **11**(2), 228–249 (2016).

[5]B. Liao, E. Najafi, H. Li, A. J. Minnich, and A. H. Zewail, "Photo-excited hot carrier dynamics in hydrogenated amorphous silicon imaged by 4D electron microscopy," Nat. Nanotechnol. **12**(9), 871–876 (2017).

[6]E. Najafi and A. Jafari, "Ultrafast imaging of surface-exclusive carrier dynamics in silicon," J. Appl. Phys. **125**(18), 185303 (2019).

[7]E. Najafi, T. D. Scarborough, J. Tang, and A. Zewail, "Four-dimensional imaging of carrier interface dynamics in p-n junctions," Science **347**(6218), 164–167 (2015).

[8]J. Cho, T. Y. Hwang, and A. H. Zewail, "Visualization of carrier dynamics in p(n)-type GaAs by scanning ultrafast electron microscopy," Proc. Natl. Acad. Sci. U. S. A. **111**(6), 2094–2099 (2014).

[9]D. S. Yang, O. F. Mohammed, and A. H. Zewail, "Environmental scanning ultrafast electron microscopy: Structural dynamics of solvation at interfaces," Angew. Chem., Int. Ed. **52**(10), 2897–2901 (2013).

[10]M. Zani, V. Sala, G. Irde, S. M. Pietralunga, C. Manzoni, G. Cerullo, G. Lanzani, and A. Tagliaferri, "Charge dynamics in aluminum oxide thin film studied by ultrafast scanning electron microscopy," Ultramicroscopy **187**, 93–97 (2018).

[11]A. M. El-Zohry, B. S. Shaheen, V. M. Burlakov, J. Yin, M. N. Hedhili, S. Shikin, B. Ooi, O. M. Bakr, and O. F. Mohammed, "Extraordinary carrier diffusion on CdTe surfaces uncovered by 4D electron microscopy," Chem **5**(3), 706–718 (2019).

[12]M. W. H. Garming, M. Bolhuis, S. Conesa-Boj, P. Kruit, and J. P. Hoogenboom, "Lock-in ultrafast electron microscopy simultaneously visualizes carrier recombination and interface-mediated trapping," J. Phys. Chem. Lett. **11**(20), 8880–8886 (2020).

[13]N. Kumar, J. He, D. He, Y. Wang, and H. Zhao, "Charge carrier dynamics in bulk MoS$_2$ crystal studied by transient absorption microscopy," J. Appl. Phys. **113**(13), 133702 (2013).

[14]M. Yabuta, A. Takeda, T. Sugimoto, K. Watanabe, A. Kudo, and Y. Matsumoto, "Particle size dependence of carrier dynamics and reactivity of photocatalyst BiVO$_4$ probed with single-particle transient absorption microscopy," J. Phys. Chem. C **121**(40), 22060–22066 (2017).

[15]W. Melitz, J. Shen, A. C. Kummel, and S. Lee, "Kelvin probe force microscopy and its application," Surf. Sci. Rep. **66**(1), 1–27 (2011).

[16]S. Yoshida, Y. Arashida, H. Hirori, T. Tachizaki, A. Taninaka, H. Ueno, O. Takeuchi, and H. Shigekawa, "Terahertz scanning tunneling microscopy for visualizing ultrafast electron motion in nanoscale potential variations," ACS Photonics **8**(1), 315–323 (2021).

[17]L. Wang, C. Xu, M. Y. Li, L. J. Li, and Z. H. Loh, "Unraveling spatially heterogeneous ultrafast carrier dynamics of single-layer WSe$_2$ by femtosecond time-resolved photoemission electron microscopy," Nano Lett. **18**(8), 5172–5178 (2018).

[18]M. K. Man, A. Margiolakis, S. Deckoff-Jones, T. Harada, E. L. Wong, M. B. Murali Krishna, J. Madéo, A. Winchester, S. Lei, R. Vajtai, P. M. Ajayan, and K. M. Dani, "Imaging the motion of electrons across semiconductor heterojunctions," Nat. Nanotechnol. **12**(1), 36–40 (2017).

[19]J. Sun, V. A. Melnikov, J. I. Khan, and O. F. Mohammed, "Real-space imaging of carrier dynamics of materials surfaces by second-generation four-dimensional scanning ultrafast electron microscopy," J. Phys. Chem. Lett. **6**(19), 3884–3890 (2015).

[20]A. Adhikari, J. K. Eliason, J. Sun, R. Bose, D. J. Flannigan, and O. F. Mohammed, "Four-dimensional ultrafast electron microscopy: Insights into an emerging technique," ACS Appl. Mater. Interfaces **9**(1), 3–16 (2017).

[21]M. Solà-Garcia, S. Meuret, T. Coenen, and A. Polman, "Electron-induced state conversion in diamond NV centers measured with pump-probe cathodoluminescence spectroscopy," ACS Photonics **7**(1), 232–240 (2020).

[22]J. Zhao, O. M. Bakr, and O. F. Mohammed, "Ultrafast electron imaging of surface charge carrier dynamics at low voltage," Struct. Dyn. **7**(2), 021001 (2020).

[23]B. Barwick, S. P. Hyun, O. H. Kwon, J. S. Baskin, and A. H. Zewail, "4D imaging of transient structures and morphologies in ultrafast electron microscopy," Science **322**(5905), 1227–1231 (2008).

[24]S. Meuret, M. Solà Garcia, T. Coenen, E. Kieft, H. Zeijlemaker, M. Lätzel, S. Christiansen, S. Y. Woo, Y. H. Ra, Z. Mi, and A. Polman, "Complementary cathodoluminescence lifetime imaging configurations in a scanning electron microscope," Ultramicroscopy **197**, 28–38 (2019).

[25]R. Bose, J. Sun, J. I. Khan, B. S. Shaheen, A. Adhikari, T. K. Ng, V. M. Burlakov, M. R. Parida, D. Priante, A. Goriely, B. S. Ooi, O. M. Bakr, and O. F. Mohammed, "Real-space visualization of energy loss and carrier diffusion in a semiconductor nanowire array using 4D electron microscopy," Adv. Mater. **28**(25), 5106–5111 (2016).

[26]R. Bose, A. Adhikari, V. M. Burlakov, G. Liu, M. A. Haque, D. Priante, M. N. Hedhili, N. Wehbe, C. Zhao, H. Yang, T. K. Ng, A. Goriely, O. M. Bakr, T. Wu, B. S. Ooi, and O. F. Mohammed, "Imaging localized energy states in silicon-doped InGaN nanowires using 4D electron microscopy," ACS Energy Lett. **3**(2), 476–481 (2018).

[27]R. Bose, A. Bera, M. R. Parida, A. Adhikari, B. S. Shaheen, E. Alarousu, J. Sun, T. Wu, O. M. Bakr, and O. F. Mohammed, "Real-space mapping of surface trap states in CIGSe nanocrystals using 4D electron microscopy," Nano Lett. **16**(7), 4417–4423 (2016).

[28]B. Liao, H. Zhao, E. Najafi, X. Yan, H. Tian, J. Tice, A. J. Minnich, H. Wang, and A. H. Zewail, "Spatial-temporal imaging of anisotropic photocarrier dynamics in black phosphorus," Nano Lett. **17**(6), 3675–3680 (2017).

[29]A. C. Zonnevylle, R. F. C. Van Tol, N. Liv, A. C. Narvaez, A. P. J. Effting, P. Kruit, and J. P. Hoogenboom, "Integration of a high-NA light microscope in a scanning electron microscope," J. Microsc. **252**(1), 58–70 (2013).

[30]A. C. Narváez, I. G. C. Weppelman, R. J. Moerland, N. Liv, A. Christiaan Zonnevylle, P. Kruit, and J. P. Hoogenboom, "Cathodoluminescence microscopy of nanostructures on glass substrates," Opt. Express **21**(24), 29968 (2013).

[31]R. J. Moerland, I. G. C. Weppelman, M. W. H. Garming, P. Kruit, and J. P. Hoogenboom, "Time-resolved cathodoluminescence microscopy with sub-nanosecond beam blanking for direct evaluation of the local density of states," Opt. Express **24**(21), 24760 (2016).

[32]M. W. H. Garming, I. G. C. Weppelman, P. De Boer, F. P. Martínez, R. Schirhagl, J. P. Hoogenboom, and R. J. Moerland, "Nanoparticle discrimination based on wavelength and lifetime-multiplexed cathodoluminescence microscopy," Nanoscale **9**(34), 12727–12734 (2017).

[33]R. J. Moerland, I. G. C. Weppelman, M. Scotuzzi, and J. P. Hoogenboom, "Nanoscale imaging of light-matter coupling inside metal-coated cavities with a pulsed electron beam," Nano Lett. **18**(10), 6107–6112 (2018).

[34]E. Najafi, V. Ivanov, A. Zewail, and M. Bernardi, "Super-diffusion of excited carriers in semiconductors," Nat. Commun. **8**, 15177 (2017).

[35]B. Liao and E. Najafi, "Scanning ultrafast electron microscopy: A novel technique to probe photocarrier dynamics with high spatial and temporal resolutions," Mater. Today Phys. **2**, 46–53 (2017).

[36]N. C. MacDonald, G. Y. Robinson, and R. M. White, "Time-resolved scanning electron microscopy and its application to bulk-effect oscillators," J. Appl. Phys. **40**(11), 4516–4528 (1969).

[37]L. Zhang, J. P. Hoogenboom, B. Cook, and P. Kruit, "Photoemission sources and beam blankers for ultrafast electron microscopy," Struct. Dyn. **6**(5), 051501 (2019).

[38]W. Verhoeven, J. F. M. van Rens, E. R. Kieft, P. H. A. Mutsaers, and O. J. Luiten, "High quality ultrafast transmission electron microscopy using resonant microwave cavities," Ultramicroscopy **188**, 85–89 (2018).

[39]L. Zhang, M. W. H. Garming, J. P. Hoogenboom, and P. Kruit, "Beam displacement and blur caused by fast electron beam deflection," Ultramicroscopy **211**, 112925 (2020).

[40]A. Castellanos-Gomez, M. Buscema, R. Molenaar, V. Singh, L. Janssen, H. S. J. Van Der Zant, and G. A. Steele, "Deterministic transfer of two-dimensional materials by all-dry viscoelastic stamping," 2D Materials **1**(1), 011002 (2014).

[41]H. Wang, C. Zhang, and F. Rana, "Surface recombination limited lifetimes of photoexcited carriers in few-layer transition metal dichalcogenide MoS_2," Nano Lett. **15**(12), 8204–8210 (2015).

[42]N. Accanto, J. B. Nieder, L. Piatkowski, M. Castro-Lopez, F. Pastorelli, D. Brinks, and N. F. Van Hulst, "Phase control of femtosecond pulses on the nanoscale using second harmonic nanoparticles," Light **3**(1), e143 (2014).

[43]M. Pawłowska, S. Goetz, C. Dreher, M. Wurdack, E. Krauss, G. Razinskas, P. Geisler, B. Hecht, and T. Brixner, "Shaping and spatiotemporal characterization of sub-10-fs pulses focused by a high-NA objective," Opt. Express **22**(25), 31496 (2014).

[44]H. Shi, R. Yan, S. Bertolazzi, J. Brivio, B. Gao, A. Kis, D. Jena, H. G. Xing, and L. Huang, "Exciton dynamics in suspended monolayer and few-layer MoS_2 2D crystals," ACS Nano **7**(2), 1072–1080 (2013).

[45]J. H. Strait, P. Nene, and F. Rana, "High intrinsic mobility and ultrafast carrier dynamics in multilayer metal-dichalcogenide MoS_2," Phys. Rev. B **90**, 245402 (2014).

[46]M. Palummo, M. Bernardi, and J. C. Grossman, "Exciton radiative lifetimes in two-dimensional transition metal dichalcogenides," Nano Lett. **15**(5), 2794–2800 (2015).

[47]Y. Li, U. Choudhry, J. Ranasinghe, A. Ackerman, and B. Liao, "Probing surface photovoltage effect using photoassisted secondary electron emission," J. Phys. Chem. A **124**(25), 5246–5252 (2020).

[48]L. Reimer, *Scanning Electron Microscopy*, 2 ed., *Springer Series in Optical Sciences* Vol. 45 (Springer, Berlin, Heidelberg, 1998).